Journal of Alloys and Compounds 968 (2023) 172078

Contents lists available at ScienceDirect

Journal of Alloys and Compounds

journal homepage: www.elsevier.com/locate/jalcom

Using neutron diffraction to explore lithium displacement within cubic phase stabilised Ga-doped $Li_{6.75}La_3Zr_{1.75}Ta_{0.25}O_{12}$ lithium garnet oxides

Timothy Daniel Christopher [a,b], Tianhang Zhang [c,d], Saifang Huang [c,e], Zoran Zujovic [a,f], Maxim Avdeev [g,h], Peng Cao [b,c], Tilo Söhnel [a,b,*]

[a] School of Chemical Sciences and Centre for Green Chemical Science, University of Auckland, Private Bag 92019, Auckland 1142, New Zealand
[b] MacDiarmid Institute for Advanced Materials and Nanotechnology, Victoria University of Wellington, PO Box 600, Wellington 6140, New Zealand
[c] Department of Chemical and Materials Engineering, University of Auckland, Private Bag 92019, Auckland 1142, New Zealand
[d] School of Materials Science and Technology, Beijing Key Laboratory of Materials, Utilisation of Nonmetallic Minerals and Solid Wastes, National Laboratory of Mineral Materials, China University of Geosciences (Beijing), Beijing 100083, PR China
[e] School of Materials Science and Engineering, Jiangsu University of Science and Technology, Zhenjiang 212003, PR China
[f] The NMR Centre, Faculty of Science, University of Auckland, Private Bag 92019, Auckland 1010, New Zealand
[g] School of Chemistry, The University of Sydney, Sydney, New South Wales 2006, Australia
[h] Australian Nuclear Science and Technology Organisation, Lucas Heights, New South Wales 2234, Australia

ARTICLE INFO

Keywords:
Ceramics
Ionic conduction
Neutron diffraction
X-ray diffraction

ABSTRACT

Typical $Li_{6.75}La_3Zr_{1.75}Ta_{0.25}O_{12}$ exists as a mixture of tetragonal and cubic arrangements, but adding small amounts of Ga^{3+} ($Li_{6.75-3x}Ga_xLa_3Zr_{1.75}Ta_{0.25}O_{12}$ $x \geq 0.1$) resulted in a single cubic (*I a-3d*) phase lithium garnet oxide. Following the stabilisation of the cubic phase, the effects on lithium distributions were explored with neutron powder diffraction concerning Ga^{3+} content and temperature. Increasing the amount of Ga^{3+} reduced the amount of lithium within the structure, directly decreasing the Li 96h site occupancy and showing a minimal effect on the Li 24d site occupancy. High-temperature neutron diffraction studies revealed the migration of lithium from the Li 24d site to the Li 96h with increasing temperature. The inclusion of Ga^{3+} improved the total ionic conductivity over the gallium-free system. However, with increasing gallium content ($x > 0.1$), a negative correlation between the garnet's gallium content and total lithium ionic conductivity is observed, showing how the total amount of free lithium ions impact the system's total ionic conductivity. Though the electrolytes explored here show some limitations, the lithium-ion displacement trends with doping and temperature give us further insight into how these lithium garnet systems respond to chemical and physical change.

1. Introduction

Incorporating volatile organic-based electrolyte components in current-generation lithium-ion batteries (LIBs) has raised serious safety concerns due to flammability and toxicity risks [1–3]. The use of a solid-state electrolyte (SSE) has been proposed as a solution to these risks. Still, issues with poor conducting performance, general stability and long-term cyclability prevent their widespread use in LIBs [4]. Next-generation LIBs will require high energy density, generous long-term cyclability, high ionic conductivity, good electronic stability with electrodes and negligible electronic conductivities [5–7].

In 2003, Thangadurai et al. reported the Li-ion conducting abilities of $Li_5La_3M_2O_{12}$ (M = Nb, Ta) with conductivity on the scale of 10^{-6} S cm^{-1} [8]. It was not until 2007 when Murugan et al. reported on the synthesis of $Li_7La_3Zr_2O_{12}$ (LLZO), a lithium garnet oxide (LGO) with a lithium ionic conductivity of $\sim 10^{-4}$ S cm^{-1} that showcased the potential use of LGO as a Li-ion SSE [9]. LLZO exists in a cubic and tetragonal arrangement, with the latter thermodynamically stable at room temperature [10,11]. The difference in structural arrangements leads to a significant change in LLZO Li-ion conductivity. The lithium-ion conductivity of the cubic and tetragonal arrangements are $\sim 10^{-4}$ S cm^{-1} and $\sim 10^{-6}$ S cm^{-1}, respectively. The tetragonal phases' lower conductivity resulted from the more localised lithium ions within the structure [9,12]. Much work has been undertaken to stabilise the higher-performing cubic arrangement at room temperature.

The LLZO cubic phase can be stabilised with elemental substitution

* Corresponding author at: School of Chemical Sciences and Centre for Green Chemical Science, University of Auckland, Private Bag 92019, Auckland 1142, New Zealand.
E-mail address: t.soehnel@auckland.ac.nz (T. Söhnel).

https://doi.org/10.1016/j.jallcom.2023.172078
Received 20 April 2023; Received in revised form 20 August 2023; Accepted 7 September 2023
Available online 9 September 2023

with typical examples of doping in the Li positions with Al^{3+}, Ga^{3+} and Fe^{3+} [13–16], or the Zr position with Ta^{5+}, $Nb^{5+}$and Y^{3+} [17–19]. The most impressive of these LGOs have achieved conductivities on the scale of $\sim 10^{-3}$ S cm^{-1}, with much work being undertaken to improve the performance of $Li_{6.75}La_3Zr_{1.75}Nb_{0.25}O_{12}$ (8×10^{-4} S cm^{-1}), $Li_{6.4}La_3Zr_{1.4}Ta_{0.6}O_{12}$ (1×10^{-3} S cm^{-1}) and $Li_{6.75}Ga_{0.25}La_3Zr_2O_{12}$ (1.46×10^{-3} S cm^{-1}) [18,20–23].

Interestingly, Ta-doping in $Li_{6.75}La_3Zr_{1.75}Ta_{0.25}O_{12}$ results in a mixture of cubic and tetragonal arrangements [10]. A sole cubic phase can be achieved by multi-doping, as reported by Meesala et al., with the use of Ba+Ta and Ga+Ba+Ta to stabilise the cubic phase and enhance the ionic conductivity [24]. Multi and co-doping have the advantage of using smaller amounts of one dopant to stabilise the cubic phase, resulting in different changes in the overall LGO lithium ion content compared to mono-doping. Higher-performing LGOs tend to have six-seven lithium atoms per chemical formula with lithium molar equivalence, producing sufficient lithium vacancies within the structure to support enhanced conductivity [25].

Multi-doping is becoming more prevalent in the literature with such combinations attempts of Al+Ta in $Li_{7-3x-y}Al_xLa_3Zr_{2-y}Ta_yO_{12}$, Y+Sb in $Li_{6.925}La_{3-x}Y_xZr_{1.925}Sb_{0.075}O_{12}$, Ba+Nb in $Li_{6+y}La_{3-y}Ba_yNbZrO_{12}$, Ca+Ta in $Li_{6.4+x}La_{3-x}Ca_xZr_{1.4}Ta_{0.6}O_{12}$, $Li_{6.6+x}La_{3-x}Ca_xZr_{1.6}Ta_{0.4}O_{12}$, Sr+Mo in $Li_{6.6+x}La_{3-x}Sr_xZr_{1.8}Mo_{0.2}O_{12}$, Sr+Nb in $Li_{6+y}La_{3-y}Sr_yNbZrO_{12}$, Ga+Sr in $Li_{6.4+x}Ga_{0.2}La_{3-x}Sr_xZr_2O_{12}$ and Ga+Ta in $Li_{6.4}Ga_{0.133}La_3Zr_{1.6}Ta_{0.2}O_{12}$ [26–33]. These synergetic attempts of co-doping have shown how to modify the total amount of lithium-ion present, which directly impacted the ionic conductivity.

Herein, we report on the LGO series of $Li_{6.75-3x}Ga_xLa_3Zr_{1.75}Ta_{0.25}O_{12}$ and explore the relationship between Ga+Ta multi-doping on the structure, lithium site occupancy and Li-ion conductivity.

2. Material and methods

2.1. Sample preparation

The series of $Li_{6.75-3x}Ga_xLa_3Zr_{1.75}Ta_{0.25}O_{12}$ of x = 0–0.5 was prepared via the standard solid-state sintering method made from stoichiometric amounts of the following precursors: Li_2CO_3 (Sigma, 99.0 %), Ga_2O_3 (Sigma, 99.9 %), La_2O_3 (Sigma, 99.9 %), ZrO_2 (Aladdin, 99.99 %) and Ta_2O_5 (Ningxia Orient Tantalum Industry CO. Ltd, > 99.9 %). La_2O_3 powder was heated at 900 °C for 12 h to remove moisture [13]. A lithium salt excess of 15 wt% was used to account for the loss of lithium vapour at higher temperatures [34]. Precursor powders were milled by a planetary mill for six hours in a stainless-steel container and lid, with zirconia milling balls and AR-grade ethanol (99.5 %). The resulting slurry was dried at 120 °C, and the retrieved powder was calcinated at 850 °C for 6 h. The calcinated powder mixture was pressed into pellets ~ 10 mm in diameter. The pellet samples were then sintered at 1100 °C for 6 h whilst covered in a sacrificial powder from the calcinated powder batch [35]. For electronic studies, the faces of the sintered pellets (~ 0.5 g) were coated with silver paste (Sigma, microparticles > 75 %) and cured at 450 °C for 30 min per side. Zirconia reaction vessels were used over the corundum to prevent Al^{3+} contamination for all heating steps. Fixed heating and cooling rates of 2 °C min^{-1} were used in all heating stages. For scanning electron miscopy and energy dispersive spectroscopy studies, samples were coated with platinum by physical vapour depositions.

2.2. Characterisation

X-ray diffraction patterns (XRD) were collected with a PANalytical Empyrean powder X-ray diffractometer with a standard CuKα_1 X-ray source of $\lambda = 1.5418$ Å, over a two-theta range of 10–90° and at room temperature. Neutron diffraction patterns were collected on the ECHIDNA High-Resolution Powder Diffractometer at the ANSTO facility in Sydney, Australia. All data collection used a neutron incident beam of

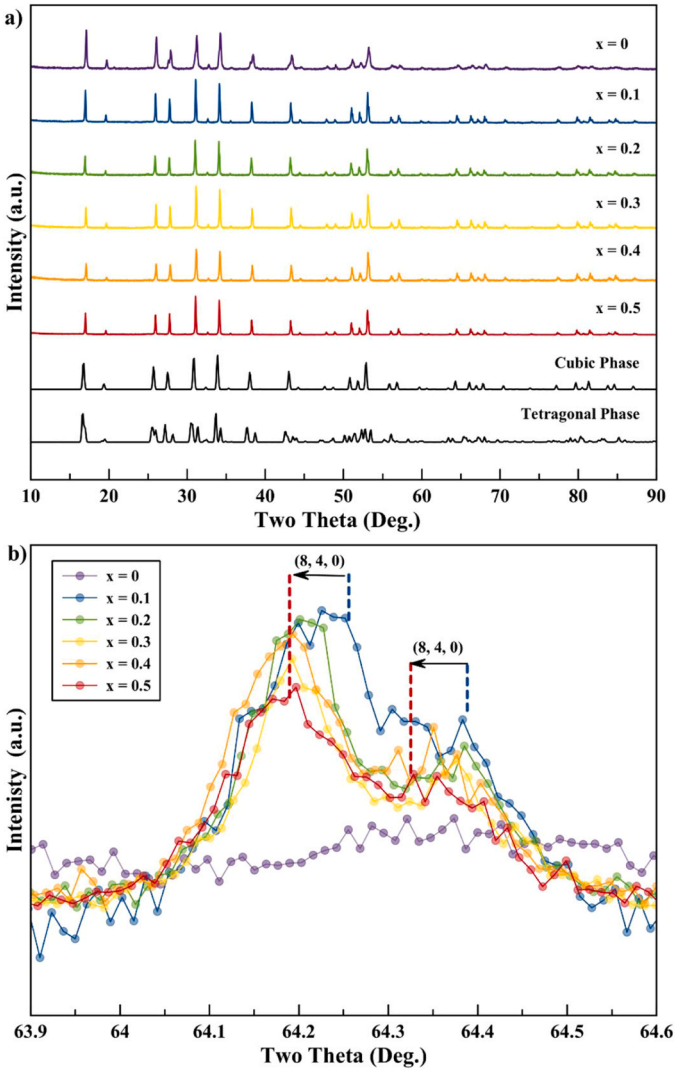

Fig. 1. a) X-ray diffraction patterns of $Li_{6.75-3x}Ga_xLa_3Zr_{1.75}Ta_{0.25}O_{12}$ series of x = 0 – 0.5 prepared at 1100 °C. Cubic reference $Li_{6.5}La_3Zr_{1.5}Ta_{0.5}O_{12}$ [39]. Tetragonal reference $Li_7La_3Zr_2O_{12}$. [20] b) Shifting hkl (8 4 0) reflections to a lower two theta (°) as a result of the increased lattice size of gallium doping in the LLZTO system.

$\lambda = 1.6215$ Å. Data collection was at room temperature (25 °C), 200 °C, 400 °C and 600 °C [36]. Structural models using the Rietveld refinement method were done using the Fullprof software [37]. Scanning electron microscopy (SEM) imagining was conducted on a FEI Quanta 200 field emission Environmental SEM at 10 keV. Energy dispersive spectroscopy spectrums were collected using an EDAX Pegasus EDS detector at 30 keV. Solid-state nuclear magnetic resonance measurements were run on a Bruker AV III HD 500 NMR spectrometer operating at the magnetic field of 11.74 T and the 194. 4 MHz frequency for ^7Li. A double-tuning probe with 4 mm zirconium oxide (ZrO_2) rotors and Kel-F caps was used. Recycle delays were determined by the saturation recovery experiments, which assured the complete relaxation of all components in the materials under investigation. The measurements were performed with a recycle delay of 1 s. The excitation pulse was 0.9 μs, 20 ms data acquisition, and a spectral width of 200 kHz. The spinning frequency was 15 kHz. The ^7Li chemical shift scale was referenced to aqueous ^7LiCl (1 M in H_2O). The number of transients was 16. The ionic conductivity and the activation energy were determined with a Biologic SP-300 Potentiostat. For each Ag/LGO/Ag cell, the frequency range was between 1 Hz and 1 MHz, all conducted at room temperature. The activation energy was calculated with the temperature-dependent relationship at 19–100 °C

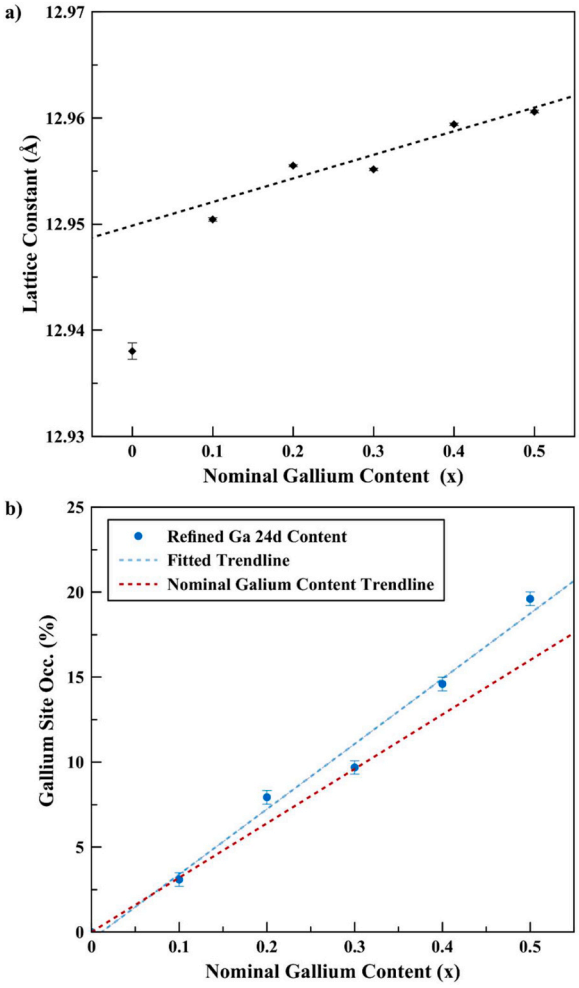

Fig. 2. a) Refined lattice parameters, (Å) versus gallium content (x) for the Ga-LLZTO series of $Li_{6.75-3x}Ga_xLa_3Zr_{1.75}Ta_{0.25}O_{12}$, x = 0–0.5. The value for x = 0 is for the cubic phase only. b) Refined gallium content in the Ga 24d site from the structural refinements from LGO $Li_{6.75-3x}Ga_xZr_{1.75}Ta_{0.25}O_{12}$ x = 0–0.5 XRD patterns.

using a KSL-1100X muffle furnace.

3. Results

3.1. Structural analysis

3.1.1. X-ray powder diffraction

The preparation of the $Li_{6.75-3x}Ga_xLa_3Zr_{1.75}Ta_{0.25}O_{12}$ series required a two step sample preparation methodology, synthesis of the powder at 850 °C and sintering as a pellet at 1100 °C. The low synthesis temperature of 850 °C would reduce lithium lost via the vapour phase; and allow smaller garnet particles to form, as it has previously been shown that increasing the synthesis temperatures increases the particle size [38]. Smaller particles before sintering of the garnet pellet would result in the formation of a more uniform and compact system.

The diffraction patterns for the $Li_{6.75-3x}Ga_xLa_3Zr_{1.75}Ta_{0.25}O_{12}$ series (x = 0 – 0.5) prepared after sintering at 1100 °C are shown in Fig. 1a. After the sintering at 1100 °C, the gallium-free variant x = 0 has a characteristic mixture of cubic (space group: *Ia*-3*d*) and tetragonal (space group: $I4_1/acd$) LGO phases of $Li_{6.75}La_3Zr_{1.75}Ta_{0.25}O_{12}$ in agreement with the literature [10]. The composition x = 0 does not produce sufficient lithium vacancies to fully stabilise the cubic garnet phase, resulting in two LGO phases, a higher tantalum content cubic phase and a lower tantalum content tetragonal phase. Only the cubic phase is

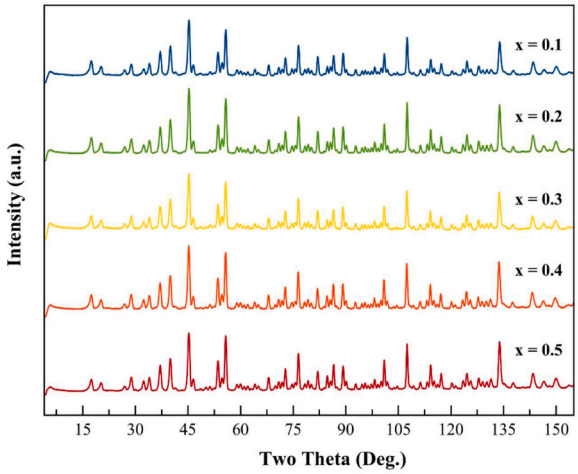

Fig. 3. Neutron powder diffraction for $Li_{6.75-3x}Ga_xZr_{1.75}Ta_{0.25}O_{12}$ (x = 0.1–0.5).

observed for the co-doped $Li_{6.75-3x}Ga_xLa_3Zr_{1.75}Ta_{0.25}O_{12}$ (x = 0.1 – 0.5). Three lithium atoms are removed for each gallium atom substituted, producing two additional site vacancies per gallium added. The lithium vacancies created with the substitution of gallium at x = 0.1 is shown to be sufficient to stabilise the cubic phase arrangement. Supporting Information Table S1 shows a list of all phases present in the X-ray refinements, with La_2O_3 present in samples x = 0.2 – 0.5 up with the maximum of a phase percentage of 1.2(7) % for x = 0.4, and $La_2Zr_2O_7$ only observed for x = 0.5 at 2.4 (1) %. Due to the lack of gallium-containing secondary phases, the addition of Ga^{3+} has shown it can stabilise the $Li_{6.75}La_3Zr_{1.75}Ta_{0.25}O_{12}$ system into a sole cubic arrangement. The presence of lithium within the Ga-LLZTO system was also confirmed with of qualitative analysis of x = 0.5 with ^7Li NMR as shown in the Supporting Information Fig. S1.

The inclusion of gallium into the cubic structure directly impacts unit cell parameters, as shown in Fig. 2a. The shifting of Bragg's reflections to a lower angle (with the (8 4 0) peaks shown as an example in Fig. 2b) reveals an increase in unit cell size, which with refined lattice parameters, a near-linear increase with gallium content is observed from 12.9504(2) Å for x = 0.1 and 12.9606(1) Å for x = 0.5. This increase in unit cell size is expected when substituting the smaller lithium (Li(I), CN = IV, 60 pm) with the larger gallium (Ga(III), CN =IV, 62 pm) [40]. Structural models of the Ga-LLZTO system revealed that gallium resides

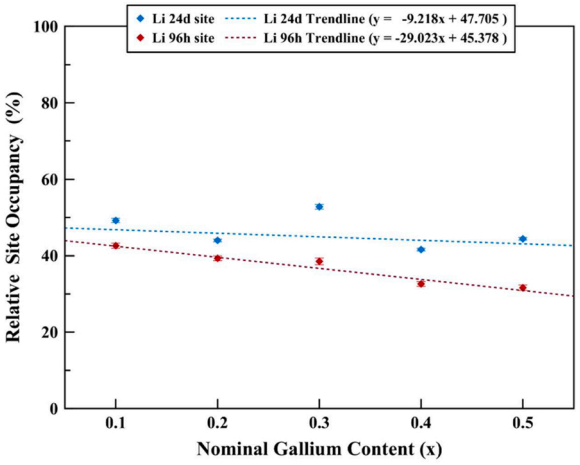

Fig. 4. Ga-LLZTO series, $Li_{6.75-3x}Ga_xZr_{1.75}Ta_{0.25}O_{12}$ (x = 0.1–0.5), Li 24d and Li 96h site occupancy percentages versus gallium content, the dotted lines serve as a guide to the eye.

Table 1
Ga and Li structural content and site occupancies for the series $Li_{6.75-3x}Ga_xZr_{1.75}Ta_{0.25}O_{12}$ (x = 0.1–0.5).

Nominal Ga Content (x)	Nominal Li Content	Refined Li Content	Ga 24d Occ. (%)	Li 24d Occ. (%)	Total 24d Occ. (%)	Percentage of Total 24d as Ga^{3+} (%)	Li 96h Occ. (%)
0.1	6.45	6.66	3.2	49.2(6)	52.4(6)	6.1	42.6(7)
0.2	6.15	6.37	6.4	44.0(4)	50.4(4)	12.7	39.3(6)
0.3	5.85	5.53	9.6	52.8(6)	62.4(6)	15.4	38.5(9)
0.4	5.55	5.14	12.8	41.6(3)	54.4(3)	23.5	32.6(6)
0.5	5.25	4.94	16.4	44.4(4)	60.8(4)	27.0	31.6(7)

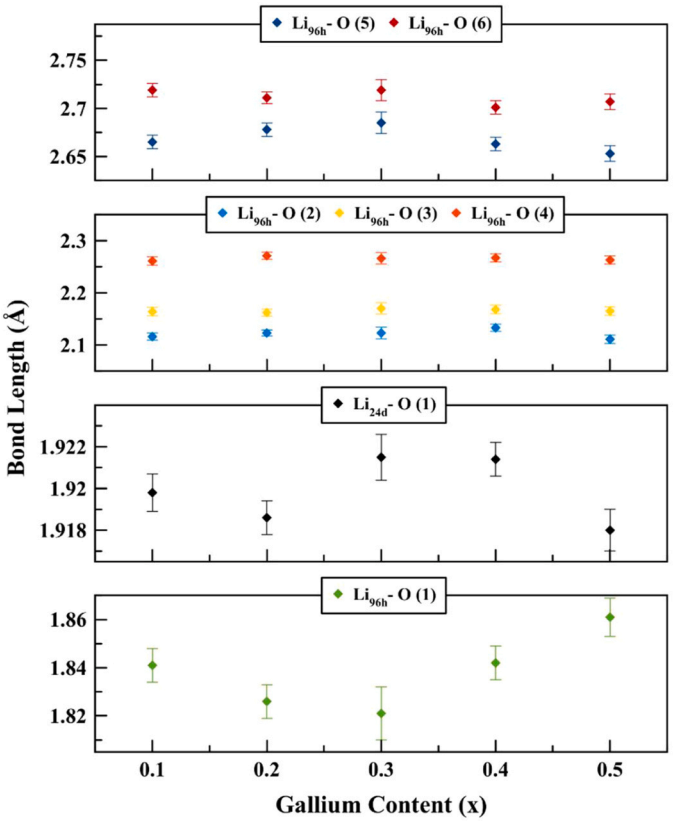

Fig. 5. Refined room temperature lithium-oxygen bond lengths for the Li 24d and Li 96h positions.

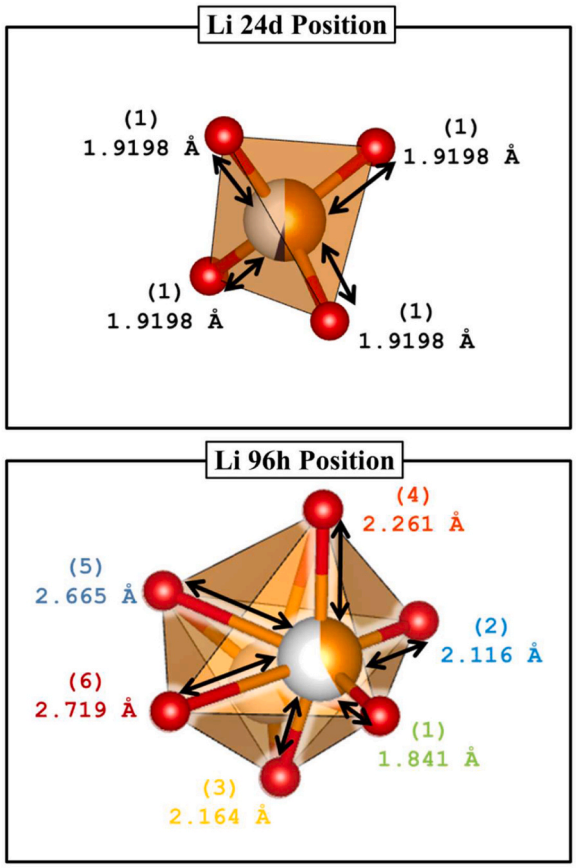

Fig. 6. Li 24d and Li 96h positions with bond lengths for $Li_{6.45}Ga_{0.1}La_3Zr_{1.75}Ta_{0.25}O_{12}$. Numbering indicates individual bond Li-O bonds used in Fig. 5.

in the tetrahedral Li 24d position, not the octahedral Li 96h position, as previously seen for other gallium-doped LLZO series [21]. This agrees with what has previously been seen for sole gallium doping and other M^{3+} doping species (e.g. Al^{3+}, Fe^{3+}) [16,22,23,41,42]. Refined Ga 24d position occupancies in Fig. 2b increase linearly and are slightly higher than the expected nominal content. As gallium is shown only to occupy the Li(Ga) 24d position, the possible effects of the lithium distribution were explored using neutron powder diffraction studies, as X-ray diffraction techniques have limitations in detecting elements with small electron densities, such as lithium.

3.2. Neutron powder diffraction

3.2.1. Room temperature studies

Neutron diffraction patterns for $Li_{6.75-3x}Ga_xZr_{1.75}Ta_{0.25}O_{12}$ (x = 0.1–0.5) in Fig. 3 all show the expected cubic phase. As the X-ray diffraction results only showed gallium occupying the Ga 24d position and did not show any gallium containing secondary phases, all neutron refinements used nominal gallium concentrations in the Ga 24d position.

The presence of gallium within the $Li_{6.75-3x}Ga_xZr_{1.75}Ta_{0.25}O_{12}$ series is significantly impacting the lithium site occupancies as shown in Fig. 4. With increasing gallium content, the occupancy of lithium in the Li 96h positions decreases from 42 % for x = 0.1 to ~ 32 % for x = 0.4 and 0.5. In comparison, the Li 24d position occupancy does decrease slightly, with the site occupancies decreasing from 47 % for x = 0.1–41 % for x = 0.4. The composition x = 0.4 is showing the lowest values of lithium positions occupancies for the LGO prepared. Removing lithium from the structure with gallium doping shows how the LGO structure maintains a critical amount of lithium in the minor tetrahedral 24d position over the larger octahedral Li 96h positions. The inclusion of gallium and lithium in the 24d positions revealed some variability in the total site occupancies, ranging from 50.4 % to 62.4 % (Table 1) for the Ga-LLZTO explored. There does appear to be some variation in the nominal and the refined lithium content, with it being slightly larger for x = 0.1, 0.2, and slightly lower for x = 0.3–0.5, but still follows the trend of decreasing lithium content with the addition of Ga. This change in lithium content and site occupancies will undoubtedly play an essential role in Ga-LLZTO's ability to conduct lithium ions.

Subtle changes in the Li-O bond lengths can be observed with the

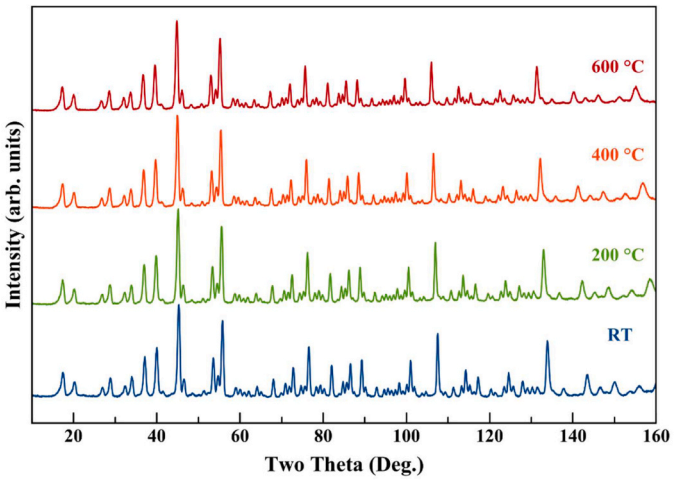

Fig. 7. Neutron powder diffraction patterns for $Li_{6.45}Ga_{0.1}La_3Zr_{1.75}Ta_{0.25}O_{12}$ from RT to 600 °C.

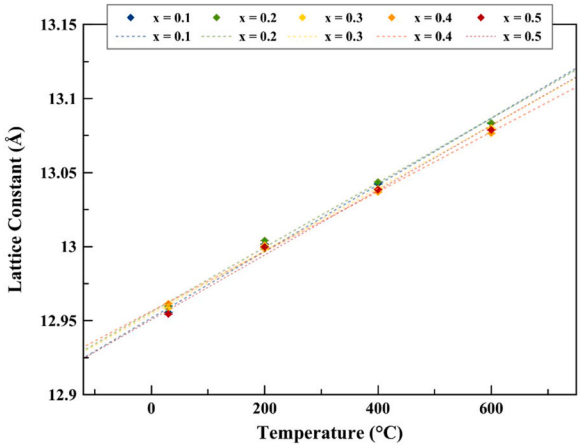

Fig. 8. Refined lattice constants (Å) versus temperature (°C) for $Li_{6.75-3x}Ga_xZr_{1.75}Ta_{0.25}O_{12}$.

increase in gallium content (Fig. 5), resulting from multiple factors. The Li 24d and Li 96h positions are coordinated in two different ways (Fig. 6). For the Li 24d position, four oxygens coordinate the tetrahedral LiO_4, all with a similar bond length. In contrast, for the Li 96h position, the octahedral LiO_6 has six oxygens with varying bond lengths depending on which side of the lithium resides on the octahedron. Li 96h position in Fig. 6 shows that the lithium is coordinated by four of the nearest oxygen atoms as shown by Li_{96h}-O bonds numbered (1)-(4) in the heavily distorted tetrahedral arrangement, and the remaining two oxygens make up the longer Li_{96h}-O bonds numbered (5) and (6). Due to the nature of the structural modelling of the Li 24d position, the inclusion of gallium will also affect the Li-O bond length. Li-O bond for the tetrahedral site appears to decrease with gallium content until x = 0.2 and increases afterwards. The increase could result from more gallium occupying the same 24d positions. As a result of powder neutron diffraction, the observed scattering of the 24d positions is a combination of the Li-O and Ga-O bonds. As seen in Table 1, the total amount of Ga^{3+} in the occupied Li/Ga24d positions (Total 24d Occ.) increases from 6.1 % to 27.0 % for x = 0.1 to x = 0.5, respectively. Each Li_{24d}-O bond length increases slightly as the larger gallium has a longer Ga-O bond length. With the octahedral Li_{96h}-O bond lengths, no fundamental distinctions can be made from some long bond lengths except for the most petite bond length, Li-O. The bond length decreases for x = 0.1–0.3 and increases from 0.3 to 0.5. This change in bond length could result from

Table 2
Linear regressions for the relationships between lattice constant Å and temperature (°C) for Fig. 8.

Gallium Content (x)	Fitted Linear Model y = Å, x = °C	R^2
0.1	y(x) = 0.00022(1)x + 12.952(4)	0.985
0.2	y(x) = 0.00022(1)x + 12.956(4)	0.9861
0.3	y(x) = 0.000212 (9)x + 12.954(3)	0.9891
0.4	y(x) = 0.000202(4)x + 12.956 (1)	0.9977
0.5	y(x) = 0.00022(1)x + 12.951(4)	0.9839

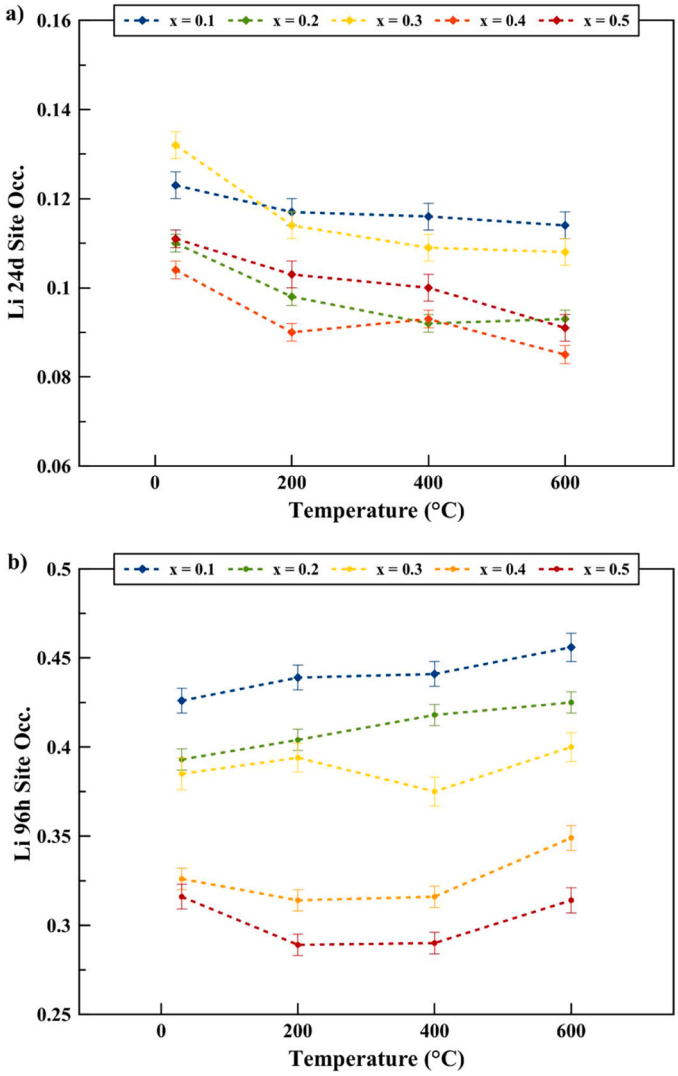

Fig. 9. Lithium site occupancies versus temperature (°C) for a) the Li 24d position and b) the Li 96d position. Max position occupancies, Li 24d: 0.250, Li 96 h: 1.00.

the neighbouring Ga 24d positions and the increasing lattice parameter. An increasing unit cell size would allow lithium to sit more tightly on one side of the Li 96h octahedral site, potentially reducing the bond lengths for Li_{96h}-O(1) and adjusting Li_{96h} -O(2) – Li_{96} -O(6). Each Li 24d tetrahedral is face-sharing with four different Li 96h octahedral, which, if containing gallium, could influence the Li 96h positions binding. For the x = 0.5 system, the Ga 24d occupancy is 16.4 % of all the 24d positions. However, 16.4 % of occupied Ga sites could influence up to 65.46 % of the total Li 96h positions. Impacting how localised the Li^+ are, as a point of interest, the refined Li 96h position occupancy for x = 0.5 is 31.6(7) %.

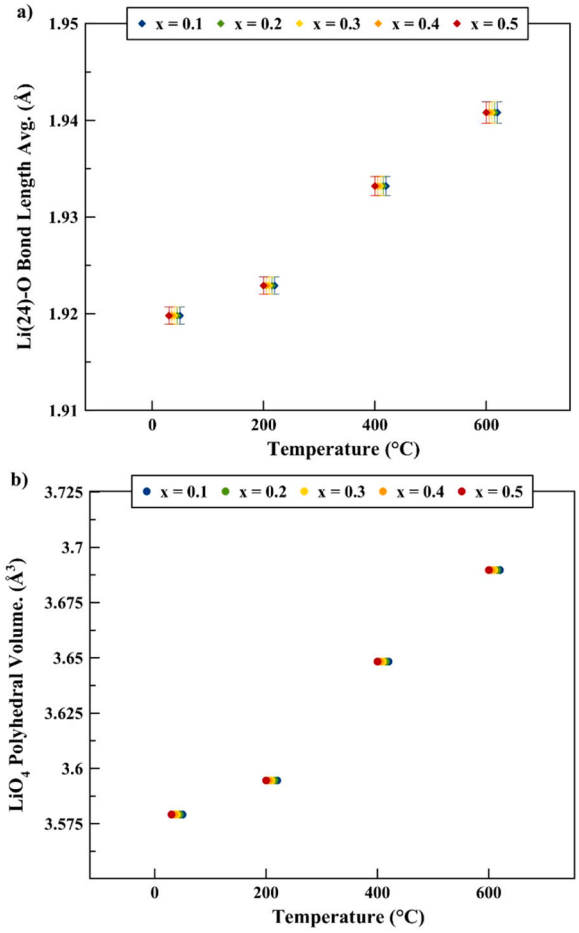

Fig. 10. a) Average lithium to oxygen bond lengths (Å) and b) LiO_4 tetrahedral volumes ($Å^3$) versus temperature (°C) for $Li_{6.75-3x}Ga_xZr_{1.75}Ta_{0.25}O_{12}$. Datasets staggered for clarity.

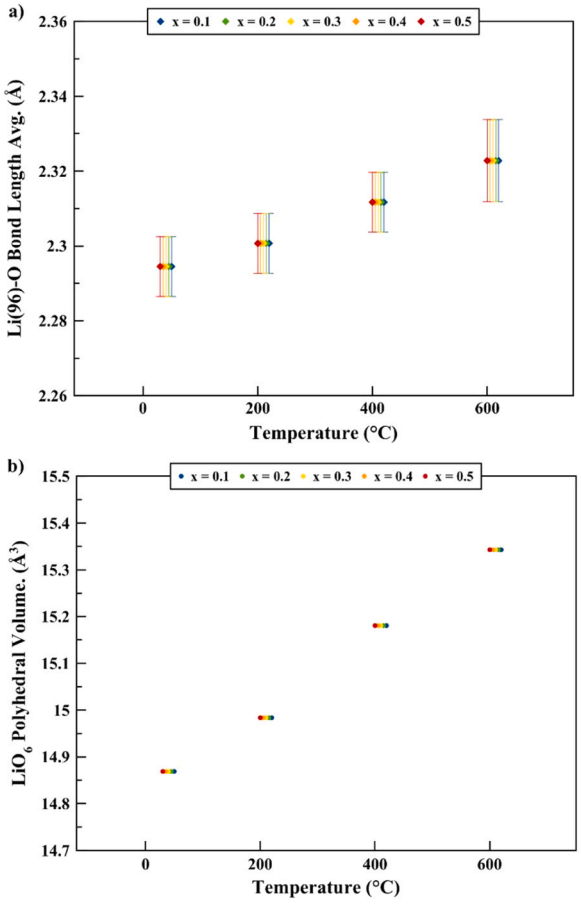

Fig. 11. (a) Average lithium to oxygen bond lengths (Å) and (b) LiO_6 octahedral volumes ($Å^3$) versus temperature (°C) for $Li_{6.75-3x}Ga_xZr_{1.75}Ta_{0.25}O_{12}$. Datasets staggered for clarity.

3.2.2. *High-temperature studies*

High-temperature neutron powder diffraction studies revealed that Ga-LLZTOs are stable up to 600 °C, the maximum temperature explored in this work, as no phase transitions or phase decomposition is seen in Fig. 7. As the cubic phase exists at room temperature, no additional thermal energy is required to stabilise the cubic system, unlike other LGO systems, such as Ge-LLZO, which require elevated temperatures to stabilise the thermal form of the cubic phase from the tetragonal phase [43]. Refined lattice parameters for the cubic (*Ia*-3*d)* systems in Fig. 8 show a linear increase in the lattice size of 2–2.2 × 10^{-4} Å/°C for all x = 0.1 – 0.5 (Table 2). With increasing thermal energy on the Ga-LLZTO system, a change in the lithium site occupancies is observed (Fig. 9). There is a difference in site volume between Li 24d and Li96h positions, with the latter being large. The Li 24d site occupancy decreases with increasing temperature, paired with an increase in the Li 96h site occupancy. With increasing thermal energy, lithium-ions migrate to a position with a larger volume to help mitigate this increase in thermal energy. Here the internal uniformity of the cubic Ga-LLZTO system does not appear to be consistent with temperature.

The changes in the average bond lengths within the Ga-LLZTO systems were also explored. Note all figures will be staggered for clarity. Fig. 10a shows the Li-O bond lengths and volumes for the Li 24d positions with a linear increase with temperature, with x = 0.5 as an example, increasing the average Li-O bond length from 1.9198(4) Å at RT to 1.940(1) Å at 600 °C (size increase of 1.05 %). This linear increase is not unexpected as the unit cell increases linearly. The same is observed for the Li-O bonds in the Li 96h positions (Fig. 11a), with the x = 0.5 again showing an increase from 2.2945(8) Å at RT and 2.323(1) Å at 600 °C (size increase of 1.24 %).

The structure of Ga-LLZTO has a backbone network of LaO_8 and Zr (Ta)O_6 polyhedra (mixed site with TaO_6). A slight change in the backbone structure of LaO_8 and ZrO_6 should be the slight difference in average Li-O bond lengths observed for the Li 24d and Li96h sites with temperature. For the average La-O bond lengths (Supporting Information Fig. S2), there is a linear increase with x = 0.5, showing an increase of 2.550(1) Å at RT to 2.579(1) Å at 600 °C (an increase of 1.14 %). For the average Zr-O bond lengths, a different trend is observed (Supporting Information Fig. S3), with them not showing a linear fashion with temperature, which appears to plateau around 400–600 °C, with average bond lengths of 2.090(1) Å at RT and 2.099(1) Å at 600 °C, only showing a 0.43 % difference.

When looking at the percentage changes in lattice parameters with doping and temperature in Table 3, it is apparent that the Zr-O bond lengths do not follow the trend of the rest of the average bond lengths in the cubic structure. The octahedral arrangement of ZrO_6 limits the expansion; thus, with further heating, we see a more significant percentage change in bond lengths with the Li-O Li 96h and La-O La 24c sites. The ZrO_6 octahedral is corner-sharing with the Li 24d sites and edge-sharing with the Li 96h sites, whereas the LaO_8 polyhedral is edge-sharing with the Li 24d sites and face-sharing with the Li 96h sites. This shows that the changes in the Li-O bond lengths seen in the Li 24d and Li 96h sites are governed by the changes in the LaO_8 polyhedra. As the LiO_4 tetrahedra (Li 24d) and distorted LiO_6 octahedra (Li 96h) share more faces, edges and corners with the LaO_8 polyhedra, the changes in average lithium bond lengths follow the changes in La-O bond length. This shows that changes in the La 24c positions could affect the lithium

Table 3
$Li_{6.75-x}Ga_xLa_3Zr_{1.75}Ta_{0.25}O_{12}$ lattice parameters, average bond length and change percentages with gallium doping and temperature. Note that values for the Li 24d site include Ga 24d, and Zr 16a includes Ta 16a.

Gallium Content (x)	Temperature (°C)	Lattice Parameter (Å)	Lattice Change (%)	Li-O (Å) (Li 24d)	Bond length Change (%)	Li-O (Å) (Li 96h)	Bond length Change (%)	La-O (Å) (La 24c)	Bond length Change (%)	Zr-O (Å) (Zr 16a)	Bond length Change (%)
0.1	30	12.9556(2)	-	1.9198 (9)	-	2.295 (8)	-	2.551(1)	-	2.090(1)	-
0.1	200	13.0016(2)	0.355	1.9229 (9)	0.161	2.301 (8)	0.270	2.562(1)	0.455	2.096(1)	0.297
0.1	400	13.0424(2)	0.670	1.933(1)	0.698	2.312 (8)	0.750	2.569(1)	0.718	2.098(1)	0.397
0.1	600	13.0834(3)	0.986	1.941(1)	1.094	2.32(1)	1.233	2.579(1)	1.106	2.099(1)	0.421
0.2	30	12.9600(1)	-	1.9198 (9)	-	2.295 (8)	-	2.550(1)	-	2.090(1)	-
0.2	200	13.0041(2)	0.342	1.9229 (9)	0.161	2.301 (8)	0.270	2.562(1)	0.455	2.096(1)	0.297
0.2	400	13.0436(2)	0.647	1.933(1)	0.698	2.312 (8)	0.750	2.569(1)	0.718	2.098(1)	0.397
0.2	600	13.0836(2)	0.955	1.941(1)	1.094	2.32(1)	1.233	2.579(1)	1.106	2.099(1)	0.421
0.3	30	12.9583(2)	-	1.9198 (9)	-	2.295 (8)	-	2.550(1)	-	2.090(1)	-
0.3	200	13.0009(2)	0.329	1.9229 (9)	0.161	2.301 (8)	0.270	2.562(1)	0.455	2.096(1)	0.297
0.3	400	13.0392(3)	0.624	1.933(1)	0.698	2.312 (8)	0.750	2.569(1)	0.718	2.098(1)	0.397
0.3	600	13.0800(3)	0.939	1.941(1)	1.094	2.323 (1)	1.233	2.579(1)	1.106	2.099(1)	0.421
0.4	30	12.9614(2)	-	1.9198 (9)	-	2.295 (8)	-	2.550(1)	-	2.090(1)	-
0.4	200	12.9986(2)	0.287	1.9229 (9)	0.161	2.301 (8)	0.270	2.562(1)	0.455	2.096(1)	0.297
0.4	400	13.0369(2)	0.582	1.933(1)	0.698	2.312 (8)	0.750	2.569(1)	0.718	2.098(1)	0.397
0.4	600	13.0766(3)	0.888	1.941(1)	1.094	2.32(1)	1.233	2.579(1)	1.106	2.099(1)	0.421
0.5	30	12.9544(2)	-	1.9198 (9)	-	2.295 (8)	-	2.550(1)	-	2.090(1)	-
0.5	200	12.9999(2)	0.351	1.9229 (9)	0.161	2.301 (8)	0.270	2.562(1)	0.455	2.096(1)	0.297
0.5	400	13.0385(3)	0.649	1.933(1)	0.698	2.312 (8)	0.750	2.569(1)	0.718	2.098(1)	0.397
0.5	600	13.0788(3)	0.960	1.941(1)	1.094	2.32(1)	1.233	2.579(1)	1.106	2.099(1)	0.421

migration from the Li 24d site to the Li 96h position, leading to changes in expected elevated lithium-ion conductivity. As a result, if these lithium garnet oxides were used in non-ambient electrochemical cells, doping with a temperature change could alter the lithium-ion distribution within the structure, resulting in varied lithium conducting abilities.

3.3. Morphology and elemental analysis

3.3.1. Scanning electron microscopy

Scanning electron micrographs of Ga-LLZTO cross-sections are shown in Fig. 12, with little to no variation in surface morphology. At the microscopic level, the cross-sections appear near-identical due to the cubic arrangements present throughout the series, except for the gallium-free (x = 0) material, which has a mixture of cubic and tetragonal arrangements. When inspecting the voids and the cleaved surface planes, the size of individual garnet crystallites is shown to be 5–10 μm in diameter. Smaller-sized crystallites can be observed trapped within large LGO domains or exposed within the void surfaces. Spherical voids can be seen, indicating pockets of trapped CO_2 gas during sintering. As there is a lack of secondary phase impurities in the diffraction analysis, the source of the CO_2 is believed to be unreacted excess Li_2CO_3.

3.3.2. Energy dispersive spectroscopy

Table 4 shows the EDS results of the detectable elements in the Ga-LLZTO series of $Li_{6.75-x}Ga_xLa_3Zr_{1.75}Ta_{0.25}O_{12}$ (x = 0–0.5). The zirconium-tantalum ratios observed agree with the X-ray refinements, where all samples show a ratio of 7-Zr:1-Ta. This ratio is supported by the mixture of cubic and tetragonal phases observed for the x = 0 system. The oxygen content varies significantly in the EDS analysis due to the smaller electronic density of oxygen (Z = 8). Weak electronic density elements such as lithium (Z = 3) do not give a signal and do not have any percentages to report. Gallium detection was completed with the Ga K lines over the Ga L lines due to overlapping between the Ga L lines and Ta M lines. Fig. 13 highlights the gallium weight percentages vs the expected gallium content for the Ga-LLZTO series. Here, the measured gallium content does follow a linear trend with gallium doping (x) but is higher than the formal gallium content.

3.4. Impedance spectroscopy analysis

3.4.1. Total ionic conductivity

Electrochemical impedance spectroscopic plots at room temperature (20 °C) for $Li_{6.75-3x}Ga_xZr_{1.75}Ta_{0.25}O_{12}$ (x = 0, 0.1, 0.2, 0.3, 0.4, 0.5) sintered at 1100 °C are shown in Fig. 14. With ionic blocking Ag electrodes, the 'tail' formation in the lower frequency range can be seen as a result of the LGO acting as an ionic conductor. Similar observations have been seen in other Ag/LGO/Ag systems explored similarly [35,44–46]. The AC impedance data show a low bulk resistance, with a grain boundary resistance being the main factor contributing to the low total ionic conductivity of the Ga-LLZTO compounds, compared with similar Ga or Ta compositions [35,44–46]. As a result, a simplified equivalent circuit of $-[R_bCPE_b][R_{gb}CPE_{gb}]CPE_{int}-$ was used to fit the plots, where *R* represents the resistance, and *CPE* is a constant phase element. Subscripted notation of *b*, *gb* and *int* represent bulk, grain boundary, and interface contributions [44]. A summary of the total ionic conductivity is

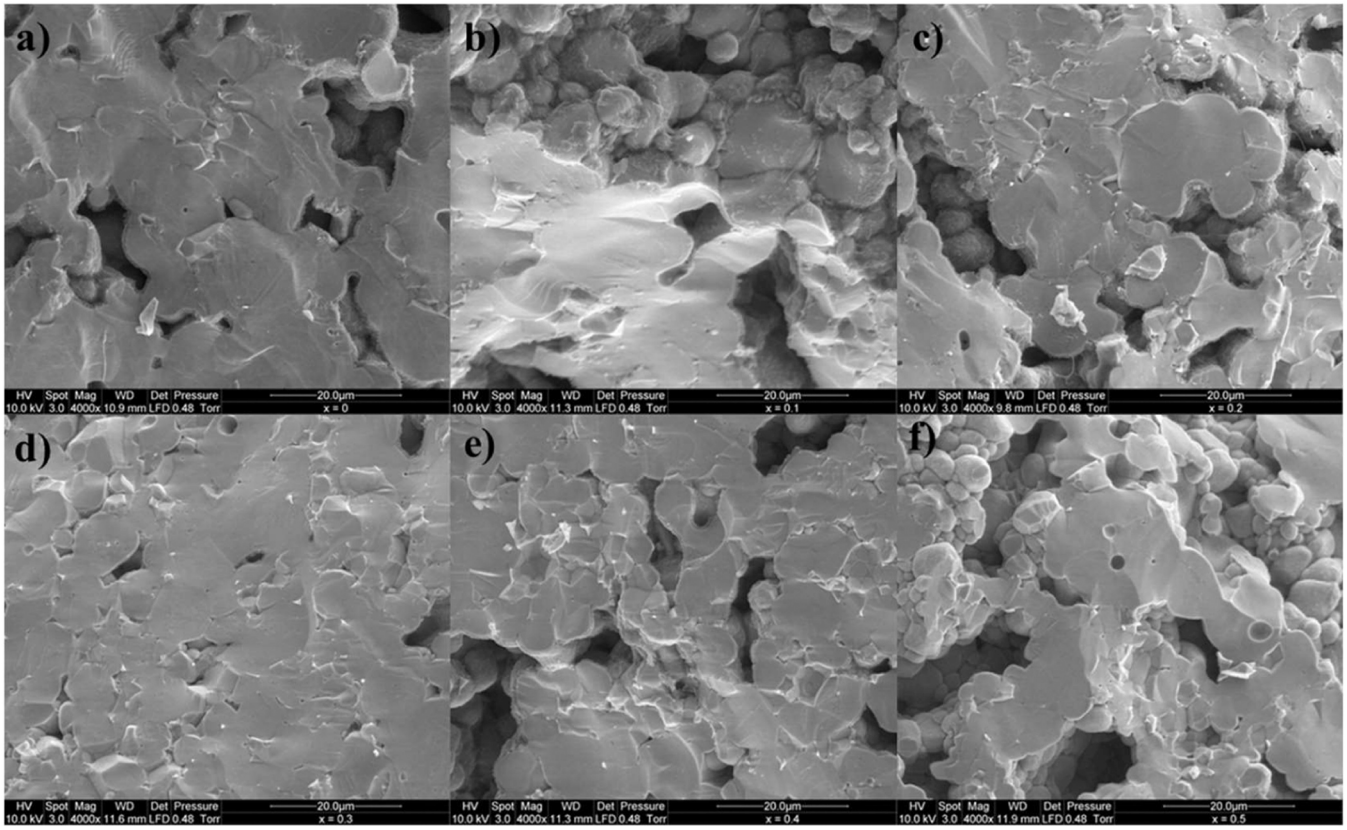

Fig. 12. Scanning electron micrographs of the Ga-LLZTO series of $Li_{6.75-x}Ga_xLa_3Zr_{1.75}Ta_{0.25}O_{12}$ with a) = 0, b) = 0.1, c) = 0.2, d) = 0.3, e) = 0.4 and f) = 0.5.

Table 4
Elemental weight percentages (wt%) for $Li_{6.75-x}Ga_xLa_3Zr_{1.75}Ta_{0.25}O_{12}$ (x = 0–0.5).

Gallium Content	Ga K (wt %)	La L (wt %)	Ta L (wt %)	Zr K (wt %)	O K (wt %)
0.0	-	46.91(3)	5.24(33)	28.54(48)	19.31 (11)
0.1	1.40(47)	41.92(5)	4.82(56)	29.34(80)	22.52 (17)
0.2	2.01(24)	44.21(3)	5.02(37)	28.36(55)	20.40 (12)
0.3	3.23(17)	42.94(4)	5.03(40)	30.36(57)	18.44 (15)
0.4	3.76(41)	41.25 (10)	4.88(103)	31.51 (140)	18.60 (39)
0.5	5.62(35)	41.60(4)	4.90(41)	30.67(57)	16.43 (15)

given in Table 5.

The total ionic conductivity (bulk + grain boundary) measured at 20 °C indicates that the ionic conductivity was enhanced with the stabilisation of the cubic phase with x = 0.1 with a maximum performance of 5.84×10^{-5} S cm^{-1} This increase can be attributed to stabilising a sole cubic phase LGO with x = 0.1, whereas the undoped x = 0 is a mixture of cubic and the low conducting tetragonal phase lithium garnet systems. With the addition of structural gallium and decreasing lithium content, the total ionic conductivity of the Ga-LZZTO system decreased to 1.46×10^{-5} S cm^{-1} for x = 0.5, as shown in Fig. 15. As the inclusion of gallium into the structure replaces lithium, it appears to affect the overall conductivity negatively, and Ga ions can block the Li-ion migration pathways through the extended system, reducing pathways for lithium-ion conduction [47].

When comparing the total conductivity of 4.5×10^{-5} S cm^{-1} for our gallium-free system, x = 0 to previously reported values of $Li_{6.75}La_3Zr_{1.75}Ta_{0.25}O_{12}$ reveals our total ionic conductivities are significantly lower than expected for this composition [48–51]. Different sample preparation conditions such as synthesis method, sintering temperature and type and concentrations of lithium additives will each impact the final product, to which the conditions explored here are less than optimal.

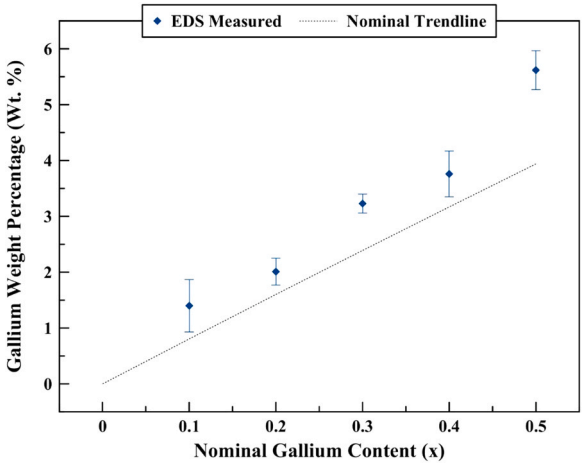

Fig. 13. Gallium weight percentage (wt%) of $Li_{6.75-x}Ga_xLa_3Zr_{1.75}Ta_{0.25}O_{12}$ (x = 0–0.5).

3.4.2. Activation energy determination

The activation energies (E_a) for the series of $Li_{6.75-3x}Ga_xZr_{1.75}Ta_{0.25}O_{12}$ of x = 0, 0.1, 0.2, 0.3, 0.4, 0.5 was determined by exploring the total ionic conductivity (σ) as a function of temperature (19 –

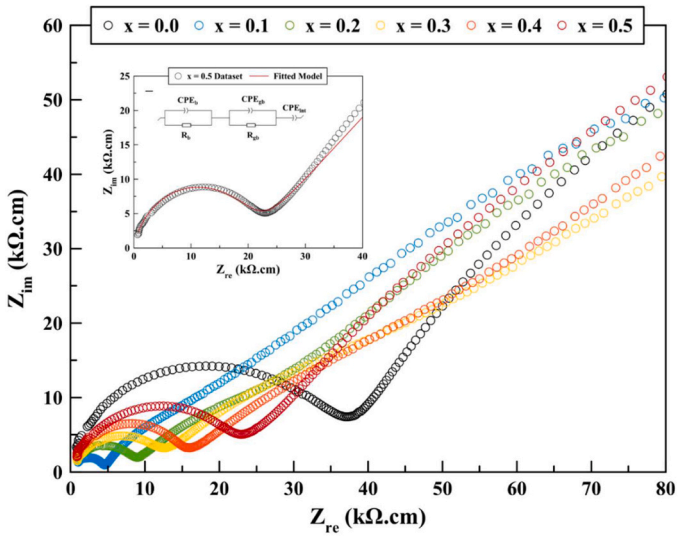

Fig. 14. Electrochemical impedance spectroscopic plots of Ag|$Li_{6.75-3x}Ga_xZr_{1.75}Ta_{0.25}O_{12}$|Ag cells, (x = 0, 0.1, 0.2, 0.3, 0.4, 0.5) series tested at room temperature (20 °C). Insert showing the fitting line for the Ag/Ga-LLZTO/Ag cell.

100 °C) with the Arrhenius equations;.

$$\sigma_{(T)} = A$$

$$Ln(\sigma_{(T)}) = Ln\ (A)$$

With *A* being constant, *k* being Boltzmann's constant, and *T* temperature in Kelvin. The temperature-dependent conductivities (σ_T) of the Ga-LLZTO series are shown in Fig. 16. From these plots, the E_a of conductivity was derived from the slope of each sample. The gallium system, of x = 0, has an E_a of 0.535(17) eV, the highest observed in this series. Regarding the inclusion of gallium a significant decrease in activation energy is observed for x > 0 and does not show any trend in the Ga-LLZTO activation energy with respect to gallium content.

3.4.3. Pellet density determination

Ga-LLZTO pellet densities were measured via the Archimedes method and compared to the calculated densities from the X-ray-sourced diffraction analysis (Table 5). With increasing gallium content, the overall density increases within the Ga-LLZTO systems. As x = 0 is the average of two cubic and tetragonal phases, with modelled densities of 5.604 and 5.090 g/$cm^{-3,}$ respectively. Across the prepared series, there is a variation in relative densities ranging from 83 % to 93 % without any apparent trend as a function of Ga doping level. Due to the use of a pressure-less sintering method, constant pressure is not forced on the materials during sintering. As a result, varying densities can be produced, evident in our sample preparation.

As mentioned, our total ionic conductivities for our x = 0 system are significantly lower than previously reported [48–51]. Differences in sample preparation conditions impact the final material, and our results show these conditions are less than optimal.

4. Conclusion

Overall, gallium doping has shown to be effective in stabilising a sole cubic phase (*Ia-3d*) $Li_{6.75-3x}Ga_xLa_3Zr_{1.75}Ta_{0.25}O_{12}$ system, which was previously shown to exist as a mixture of the cubic and tetragonal phase. Doping of gallium into the $Li_{6.75-3x}Ga_xLa_3Zr_{1.75}Ta_{0.25}O_{12}$ series was successful from x = 0.1 to x = 0.5. Diffraction studies revealed that Ga^{3+} ions were shown to replace Li^+ with a preference for the Li 24d position over the Li 96h site. High-temperature neutron studies showcase lithium migration from the Li 24d to the Li 96h positions with temperature. With temperature, not all polyhedra expand uniformly, with the ZrO_6 polyhedra being the most rigid. The doping of gallium did improve the total ionic conductivity of this system with a maximum performance of 5.84×10^{-5} S cm^{-1} for $Li_{6.45}Ga_{0.1}La_3Zr_{1.75}Ta_{0.25}O_{12}$ (x = 0.1). Though a decrease in overall E_a for the gallium-doped materials was observed, the addition of gallium content does hinder the overall ionic conductivity of the $Li_{6.75-3x}Ga_xLa_3Zr_{1.75}Ta_{0.25}O_{12}$ series. In summary, exploring this gallium and tantalum system has shown insight into lithium-ion behaviour within the lithium garnet system concerning chemical doping, temperature and resulting electrochemical performance.

CRediT authorship contribution statement

Timothy Daniel Christopher: Conceptualization, Methodology, Data curation, Formal analysis, Writing – original draft. **Tianhang Zhang:** Methodology. **Saifang Huang:** Supervision, Conceptualization. **Zoran Zujovic:** Data curation, Writing – review & editing. **Maxim Avdeev:** Data curation, Writing – review & editing. **Peng Cao:** Supervision. **Tilo Söhnel:** Conceptualization, Supervision, Writing – review &

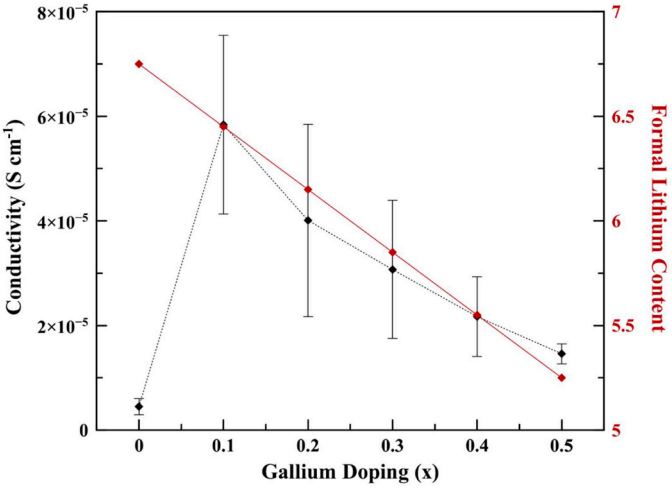

Fig. 15. Ga-LLZTO series of $Li_{6.75-3x}Ga_xZr_{1.75}Ta_{0.25}O_{12}$, (x = 0, 0.1, 0.2, 0.3, 0.4, 0.5) series conductivity (S cm^{-1}) versus gallium doping, paired with formal lithium content.

Table 5
Total ionic conductivity (S cm^{-1}), activation energy and relative densities for $Li_{7-3x}Ga_xLa_3Zr_{1.75}Ta_{0.25}O_{12}$ (x = 0–0.5). The average value for x = 0 is due to the cubic and tetragonal phases.

Gallium Content (x)	Ionic Conductivity (total) (S cm^{-1})	Std Dv (S cm^{-1})	Activation Energy Ea (eV)	Measured Density (g/cm^3)	Modelled Density (g/cm^3)	Relative Density (%)
0	4.50×10^{-6}	1.55×10^{-6}	0.535(17)	4.587*	5.387*	90.1
0.1	5.84×10^{-5}	1.81×10^{-5}	0.348(4)	4.351	5.211	83.5
0.2	4.01×10^{-5}	1.84×10^{-5}	0.367(8)	4.768	5.313	89.7
0.3	3.07×10^{-5}	1.32×10^{-5}	0.349(13)	4.698	5.376	87.4
0.4	2.17×10^{-5}	7.65×10^{-6}	0.350(4)	5.058	5.395	93.4
0.5	1.46×10^{-5}	1.90×10^{-6}	0.377(7)	4.770	5.454	87.4

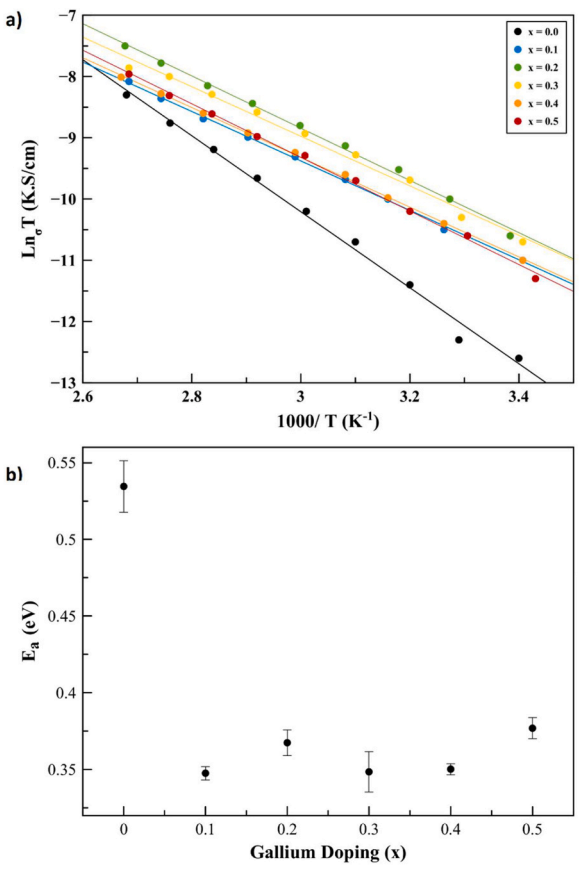

Fig. 16. a) Temperature dependency of total ionic conductivity in the Ag|$Li_{6.75-3x}Ga_xZr_{1.75}Ta_{0.25}O_{12}$|Ag cells (x = 0, 0.1, 0.2, 0.3, 0.4, 0.5) cells and b) Ga-LLZTO activation energies (E_a) versus gallium content (x). The testing temperatures were from room temperature to 100 °C at an interval of 10 °C.

editing.

Declaration of Competing Interest

The authors declare that they have no known competing financial interests or personal relationships that could have appeared to influence the work reported in this paper.

Data availability

Data will be made available on request.

Acknowledgements

Funding and support from the Australian Nuclear Science and Technology Organisation (ANSTO) for neutron powder diffraction on the ECHIDNA beamline (P7504). The UoA Shared Research Equipment Platform (ShaRe) for collecting powder X-ray diffraction data. T.C. acknowledges the University of Auckland Doctoral Scholarship.

Appendix A. Supporting information

Supplementary data associated with this article can be found in the online version at doi:10.1016/j.jallcom.2023.172078.

References

[1] J.B. Goodenough, K.-S. Park, The Li-ion rechargeable battery: a perspective, J. Am. Chem. Soc. 135 (4) (2013) 1167–1176.
[2] Y. Chen, et al., A review of lithium-ion battery safety concerns: the issues, strategies, and testing standards, J. Energy Chem. 59 (2021) 83–99.
[3] X. Wu, et al., Safety issues in lithium ion batteries: materials and cell design, Front. Energy Rev. 7 (2019).
[4] W. Zhao, et al., Solid-state electrolytes for lithium-ion batteries: fundamentals, challenges and perspectives, Electrochem. Energy Rev. 2 (4) (2019) 574–605.
[5] K. Takada, Progress and prospective of solid-state lithium batteries, Acta Mater. 61 (3) (2013) 759–770.
[6] J.W. Fergus, Ceramic and polymeric solid electrolytes for lithium-ion batteries, J. Power Sources 195 (15) (2010) 4554–4569.
[7] M. Tatsumisago, M. Nagao, A. Hayashi, Recent development of sulfide solid electrolytes and interfacial modification for all-solid-state rechargeable lithium batteries, J. Asian Ceram. Soc. 1 (1) (2013) 17–25.
[8] V. Thangadurai, H. Kaack, W.J.F. Weppner, Novel fast lithium ion conduction in garnet-type Li5La3M2O12 (M = Nb, Ta), J. Am. Ceram. Soc. 86 (3) (2003) 437–440.
[9] R. Murugan, V. Thangadurai, W. Weppner, Fast lithium ion conduction in garnet-type Li7La3Zr2O12, Angew. Chem. Int. Ed. 46 (41) (2007) 7778–7781.
[10] T. Thompson, et al., Tetragonal vs. cubic phase stability in Al – free Ta doped Li7La3Zr2O12 (LLZO), J. Mater. Chem. A 2 (33) (2014) 13431–13436.
[11] H. Buschmann, et al., Structure and dynamics of the fast lithium ion conductor "Li7La3Zr2O12", Phys. Chem. Chem. Phys. 13 (43) (2011) 19378–19392.
[12] J. Awaka, et al., Synthesis and structure analysis of tetragonal Li7La3Zr2O12 with the garnet-related type structure, J. Solid State Chem. 182 (8) (2009) 2046–2052.
[13] N. Janani, et al., Influence of sintering additives on densification and Li+ conductivity of Al doped Li7La3Zr2O12 lithium garnet, RSC Adv. 4 (93) (2014) 51228–51238.
[14] Y. Jin, P.J. McGinn, Al-doped Li7La3Zr2O12 synthesized by a polymerized complex method, J. Power Sources 196 (20) (2011) 8683–8687.
[15] J. Wolfenstine, et al., Synthesis and high Li-ion conductivity of Ga-stabilized cubic Li7La3Zr2O12, Mater. Chem. Phys. 134 (2) (2012) 571–575.
[16] R. Wagner, et al., Fast Li-ion-conducting garnet-related Li7–3xFexLa3Zr2O12 with uncommon I4¯3d structure, Chem. Mater. 28 (16) (2016) 5943–5951.
[17] Y.X. Wang, A. Huq, W. Lai, Insight into lithium distribution in lithium-stuffed garnet oxides through neutron diffraction and atomistic simulation: Li7-xLa3Zr2-xTaxO12 (x=0-2) series, Solid State Ion. 255 (2014) 39–49.
[18] S. Ohta, T. Kobayashi, T. Asaoka, High lithium ionic conductivity in the garnet-type oxide Li7−X La3(Zr2−X, NbX)O12 (X = 0–2), J. Power Sources 196 (6) (2011) 3342–3345.
[19] R. Murugan, S. Ramakumar, N. Janani, High conductive yttrium doped Li7La3Zr2O12 cubic lithium garnet, Electrochem. Commun. 13 (12) (2011) 1373–1375.
[20] A. Logéat, et al., From order to disorder: the structure of lithium-conducting garnets Li7 − xLa3TaxZr2 − xO12 (x = 0–2), Solid State Ion. 206 (2012) 33–38.
[21] J.-F. Wu, et al., Gallium-doped Li7La3Zr2O12 garnet-type electrolytes with high lithium-ion conductivity, ACS Appl. Mater. Interfaces 9 (2) (2017) 1542–1552.
[22] L. Robben, et al., Symmetry reduction due to gallium substitution in the garnet Li6.43(2)Ga0.52(3)La2.67(4)Zr2O12, Acta Crystallgr. Sect. E Crystallogr. Commun. 72 (2016) 287–289.
[23] R. Jalem, et al., Effects of gallium doping in garnet-type Li7La3Zr2O12 solid electrolytes, Chem. Mater. 27 (8) (2015) 2821–2831.
[24] Y. Meesala, et al., An efficient multi-doping strategy to enhance Li-ion conductivity in the garnet-type solid electrolyte Li7La3Zr2O12, J. Mater. Chem. A 7 (14) (2019) 8589–8601.
[25] V. Thangadurai, S. Narayanan, D. Pinzaru, Garnet-type solid-state fast Li ion conductors for Li batteries: critical review, Chem. Soc. Rev. 43 (13) (2014) 4714–4727.
[26] D.O. Shin, et al., Synergistic multi-doping effects on the Li7La3Zr2O12 solid electrolyte for fast lithium ion conduction, Sci. Rep. 5 (1) (2015) 18053.
[27] Z. Cao, et al., Y and Sb co-doped Li7La3Zr2O12 electrolyte for all solid-state lithium batteries, Ionics 27 (5) (2021) 1861–1870.
[28] T. Zhang, et al., Electrochemical properties of Li6+yLa3−yBayNbZrO12 lithium garnet oxide solid-state electrolytes with co-doping barium and zirconium, J. Alloy. Compd. 862 (2021), 158600.
[29] C. Wang, et al., Synergistic impacts of Ca2+ and Ta5+ dopants on electrical performance of garnet-type electrolytes, J. Alloy. Compd. 879 (2021), 160420.
[30] X. Zhou, et al., Sr2+ and Mo6+ co-doped Li7La3Zr2O12 with superior ionic conductivity, J. Alloy. Compd. 891 (2022), 161906.
[31] T. Zhang, et al., The influence of co-doping strontium and zirconium on structure and ionic conductivities of Li6+yLa3−ySryNbZrO12 solid electrolytes, Int. J. Mod. Phys. B 34 (01n03) (2020), 2040006.
[32] L. Shen, et al., Preparation and characterization of Ga and Sr co-doped Li7La3Zr2O12 garnet-type solid electrolyte, Solid State Ion. 339 (2019), 114992.
[33] E. Enkhbayar, J. Kim, Study of codoping effects of Ta5+ and Ga3+ on garnet Li7La3Zr2O12, ACS Omega 7 (50) (2022) 47265–47273.
[34] K. Liu, J.-T. Ma, C.-A. Wang, Excess lithium salt functions more than compensating for lithium loss when synthesizing Li6.5La3Ta0.5Zr1.5O12 in alumina crucible, J. Power Sources 260 (2014) 109–114.
[35] T. Zhang, et al., Pressureless sintering of Al-free Ta-doped lithium garnets Li7-xLa3Zr2-xTaxO12 and the degradation mechanism in humid air, Ceram. Int. 45 (16) (2019) 20954–20960.
[36] M.H. Avdeev, J.R. Hester, ECHIDNA: a decade of high-resolution neutron powder diffraction at OPAL, J. Appl. Crystallogr. 51 (2018) 1597–1604.
[37] J. Rodriguez-Carvajal, Recent developments of the program FULLPROF, commission on powder diffraction, IUCr Newsl. (2001) **26**.

[38] X. Huang, et al., Synthesis of Ga-doped Li7La3Zr2O12 solid electrolyte with high Li + ion conductivity, Ceram. Int. 47 (2) (2021) 2123–2130.
[39] S. Adams, R.P. Rao, Ion transport and phase transition in $Li_{7-x}La_3(Zr_{2-x}M_x)O_{12}$ (M = Ta^{5+}, Nb^{5+}, x=0, 0.25), J. Mater. Chem. 22 (4) (2012) 1426–1434.
[40] L. Pauling, The sizes of ions and the structure of ionic crystals, J. Am. Chem. Soc. 49 (3) (1927) 765–790.
[41] E. Rangasamy, J. Wolfenstine, J. Sakamoto, The role of Al and Li concentration on the formation of cubic garnet solid electrolyte of nominal composition Li7La3Zr2O12, Solid State Ion. 206 (2012) 28–32.
[42] M.A. Howard, et al., Effect of Ga incorporation on the structure and Li ion conductivity of La3Zr2Li7O12, Dalton Trans. 41 (39) (2012) 12048–12053.
[43] M. Kotobuki, et al., Study on stabilization of cubic Li7La3Zr2O12 by Ge substitution in various atmospheres, Funct. Mater. Lett. 09 (06) (2016) 1642005.
[44] T. Thompson, et al., A tale of two sites: on defining the carrier concentration in garnet-based ionic conductors for advanced Li batteries, Adv. Energy Materials 5 (11) (2015), 1500096.
[45] L. Dhivya, R. Murugan, Effect of simultaneous substitution of Y and Ta on the stabilization of cubic phase, microstructure, and Li+ conductivity of Li7La3Zr2O12 lithium garnet, ACS Appl. Mater. Interfaces 6 (20) (2014) 17606–17615.
[46] J.L. Allen, et al., Effect of substitution (Ta, Al, Ga) on the conductivity of Li7La3Zr2O12, J. Power Sources 206 (2012) 315–319.
[47] N. Birkner, et al., Gallium-doping effects on structure, lithium-conduction, and thermochemical stability of Li7-3xGaxLa3Zr2O12 garnet-type electrolytes, Chemsuschem 14 (12) (2021) 2621–2630.
[48] Densification and lithium ion conductivity of garnet-type Li7−xLa3Zr2−xTaxO12 (x = 0.25) solid electrolytes, Chin. Phys. B 22 (7) (2013), 078201.
[49] Y. Li, Y. Cao, X. Guo, Influence of lithium oxide additives on densification and ionic conductivity of garnet-type Li6.75La3Zr1.75Ta0.25O12 solid electrolytes, Solid State Ion. 253 (2013) 76–80.
[50] Y. Tian, et al., Li6.75La3Zr1.75Ta0.25O12@amorphous Li3OCl composite electrolyte for solid state lithium-metal batteries, Energy Storage Mater. 14 (2018) 49–57.
[51] X. Zhang, T.-S. Oh, J.W. Fergus, Densification of Ta-doped garnet-type Li6.75La3Zr1.75Ta0.25O12 solid electrolyte materials by sintering in a lithium-rich air atmosphere, J. Electrochem. Soc. 166 (15) (2019) A3753.